Beyond Mahan-Sofo Best Thermoelectric: High Thermoelectric Performance from Directional π-Conjugation in Two-Dimensional Poly(tetrathienoanthracene)

Tianqi Deng[a], Xue Yong[a], Wen Shi[a], Zicong Marvin Wong[a], Gang Wu[a], Hui Pan[b], Jian-Sheng Wang[c] and Shuo-Wang Yang[a]*

[a.] Institute of High Performance Computing, Agency for Science, Technology and Research, 1 Fusionopolis Way, #16-16 Connexis, Singapore 138632

[b.] Institute of Applied Physics and Materials Engineering, and Department of Physics and Chemistry, Faculty of Science and Technology, University of Macau, Macao SAR

[c.] Department of Physics, Faculty of Science, National University of Singapore, 2 Science Drive 3, Singapore 117551

Corresponding Author

*Email: yangsw@ihpc.a-star.edu.sg

Supporting Information

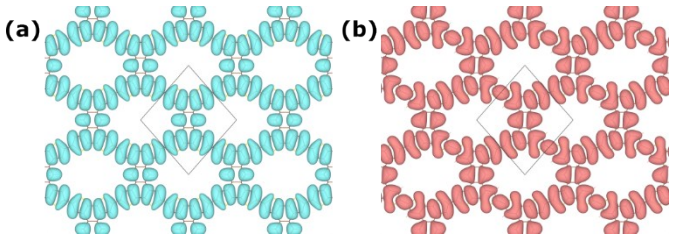

Figure S1 The valence band charge density contribution (squared modulus of wave function) of the hypothetical isomer of PTTA from (a) Γ point and (b) Σ point, respectively. Both states show extensive conjugation in two dimensions, which is very different from the case of experimentally synthesized PTTA structure.

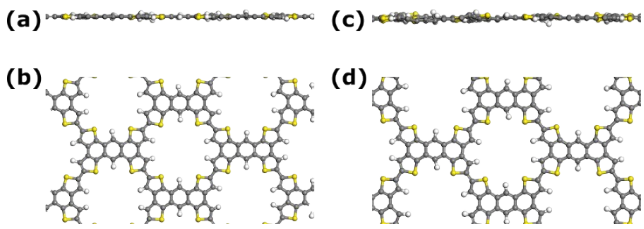

Figure S2 (a) The side and (b) top views of 2D PTTA structure after 13 ps *ab initio* molecular dynamics simulation in NVT ensemble at 300 K. (c) The side and (d) top views of 2D PTTA structure after 6 ps *ab initio* molecular dynamics simulation in NVT ensemble at 600 K. The conservation of the planarity supports PTTA's thermodynamic stability at finite temperatures.

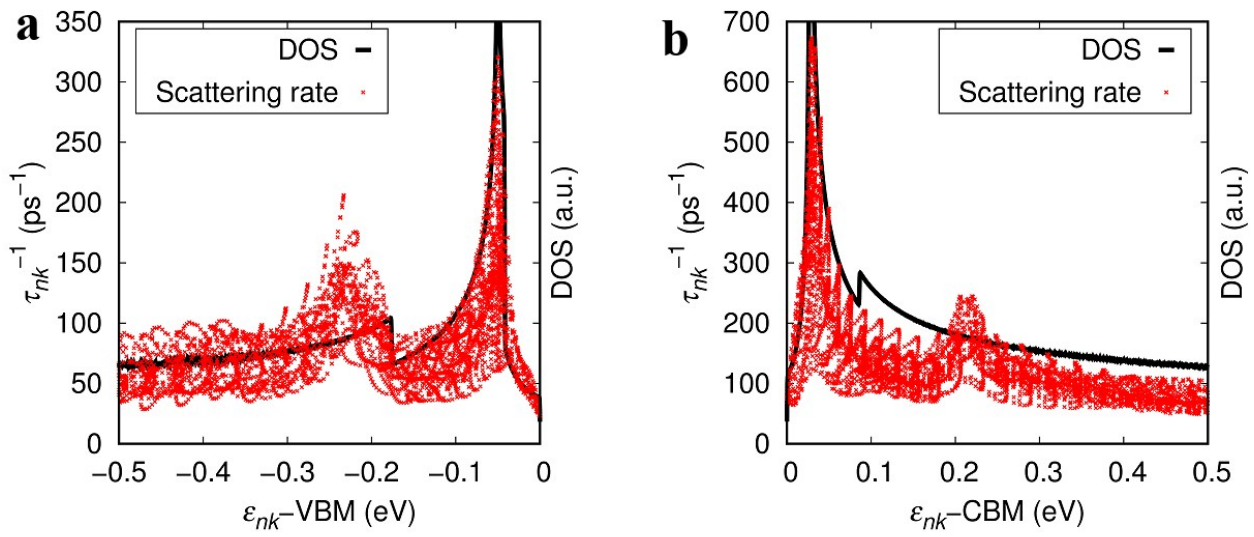

Figure S3. The phonon-limited scattering rate for states in **(a)** valence and **(b)** conduction bands, respectively for 2D PTTA.

The impurity-limited electron scattering rate, which is proportional to the density of impurities in Thomas Fermi screening approximation, is shown in Figure S4. Here n_{imp} is the average number of impurities per unit cell.

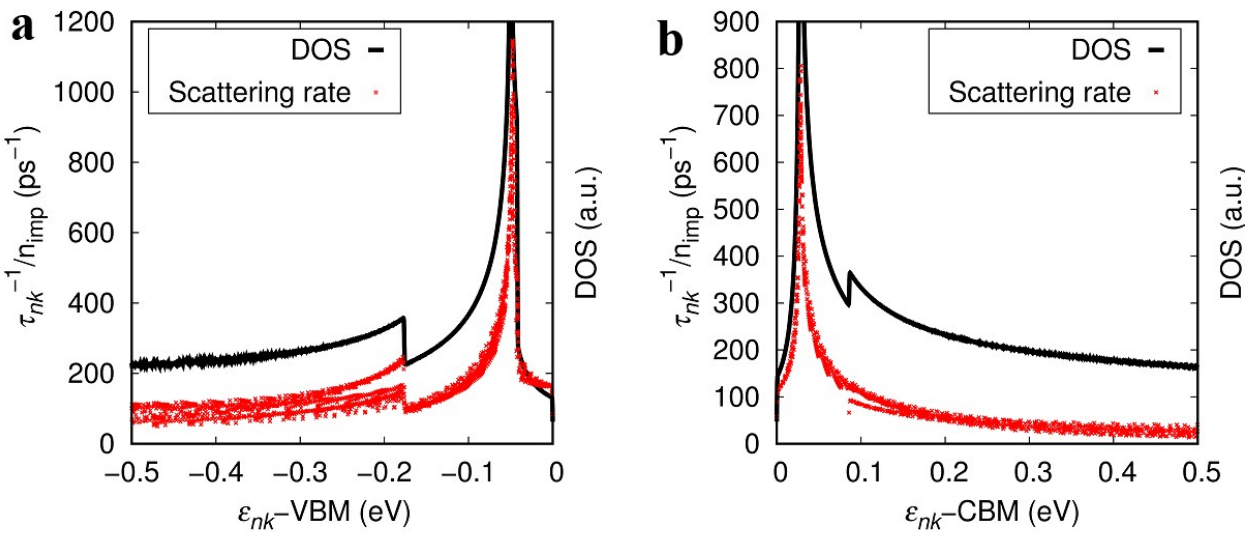

Figure S4. Ratio between impurity-limited scattering rate and average number of impurities per unit cell of PTTA, for **(a)** valence and **(b)** conduction bands.

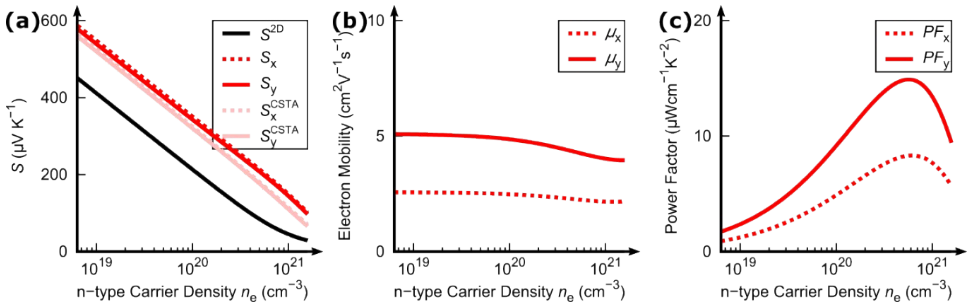

Figure S5 (a) Seebeck coefficient, (b) electron mobility, and (c) power factor of PTTA with n-type doping at 300 K. Seebeck coefficient is still higher than that from 2D parabolic band model, demonstrating the significance of DOS peak that also appears near the conduction band edge.

Conduction band structure

The conduction band also possesses ridge-like structure similar to the case of valence band shown in Figure 1g. The three-dimensional visualization of first conduction band is given in Figure S6 below, together with the squared modulus of wave functions at Γ and S points which show similar coexistence of 1D and 2D states.

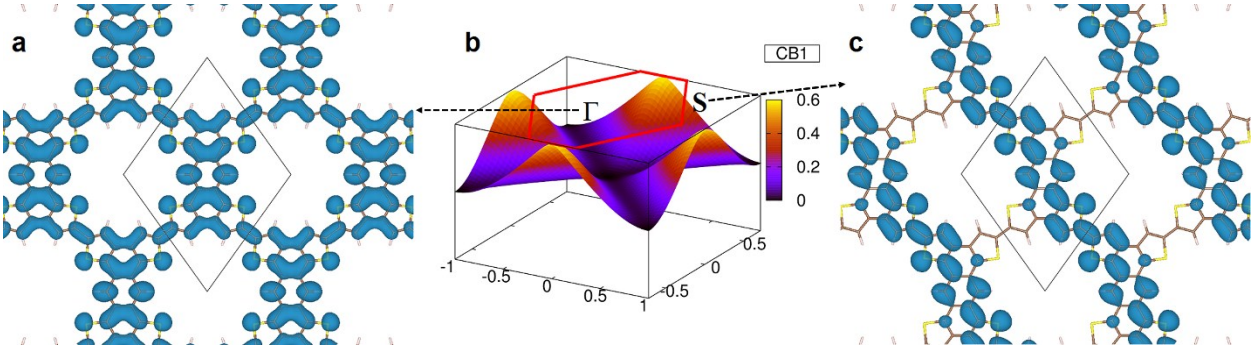

Figure S6. **(a)**Squared modulus of wave function ($|\psi(r)|^2$) for the first conduction band at Γ point. The π electron conjugation extends to all connecting repeating units. **(b)** Three-dimensional visualization of first conduction band dispersion. A ridge-like dispersion is found near zone boundary S point. **(c)** $|\psi(r)|^2$ for the first conduction band at S point. The π electron conjugation extends only along para direction, exhibiting quasi-1D confinement which corresponds to the ridge-like band structure near S point and the singularity in DOS.

Stacking of 2D PTTA layer

Here we optimized the structure of three types of stacking order for 2D PTTA, the direct on-top stacking (AA), the alternating stacking similar to Bernal stacking of graphene (AB), and monoclinic stacking where each layer is translated by the same vector (ABC). The optimized atomic structures are shown in Figure S7. The optimized lattice parameters for AA-, AB- and ABC-stacked PTTA, using D2[1] and D3[2] van der Waals corrections for dispersion interactions, are given in Table S1. Despite the slight differences in lattice constants and binding energy, the results from both D2 and D3 corrections imply that AB- and ABC-stacking are more stable than AA-stacking, while the difference between AB- and ABC-stacking is less discernible.

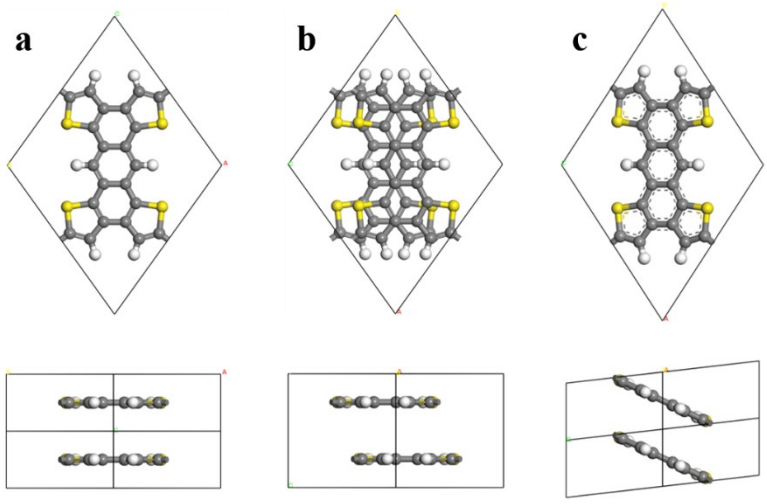

Figure S7. Top and side views of atomic structure for **(a)** AA-, **(b)** AB- and **(c)** ABC- stacked 2D PTTA. Primitive cells are shown instead of conventional cells. AA- and ABC-stacked 2D PTTA are shown as supercells to visualize the relative position of neighboring layers.

Table S1. The space groups and lattice constants (*a, b, c, β*) for three different stacking orders in conventional cell. The interlayer distances *d*, and the interlayer binding energy ΔE defined as per layer energy difference between isolated layer and stacked layers, are also given.

	stacking	space group	*a* (Å)	*b* (Å)	*c* (Å)	*β* (°)	*d* (Å)	ΔE (eV)
PBE-D2	AA	Orthorhombic *Cmmm*	14.06	19.55	3.75	90	3.75	-0.757
	AB	Orthorhombic *Cmcm*	14.05	19.55	6.80	90	3.40	-1.078
	ABC	Monoclinic *C2/m*	12.76	19.55	3.76	96.6	3.36	-1.083
PBE-D3	AA	Orthorhombic *Cmmm*	14.09	19.53	3.84	90	3.84	-0.829
	AB	Orthorhombic *Cmcm*	14.09	19.54	7.14	90	3.57	-1.046
	ABC	Monoclinic *C2/m*	12.83	19.54	3.94	98.1	3.37	-1.052

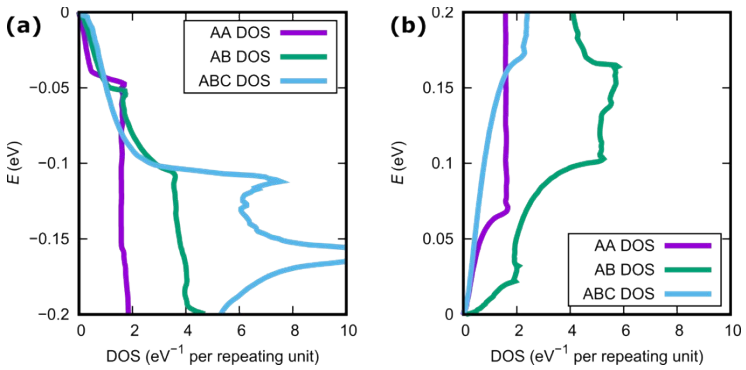

Figure S8. Electron density-of-states of AA-, AB- and ABC-stacked 2D PTTA near **(a)** valence and **(b)** conduction band edges.

In all three stacking orders studied here, the density-of-states near the band edges shows an increase that is different from three-dimensional parabolic band, as shown in Figure S8. A sharp increase near valence band edge appears around -0.05 eV for AA- and AB-stacked 2D PTTA, which is similar to the case of single layer. Meanwhile, the feature near -0.1 eV is more prominent for ABC-stacked PTTA. Despite such difference in peak position due to different inter-layer interaction, sharp increase is observed in valence band for all three stacking orders studied here, suggesting bulk layered PTTA to be a potential TE material where Seebeck enhancement due to Mahan-Sofo theory can be expected.

The peaks in conduction band of AA- and AB-stacked PTTA are similar to the case of valence band, while the increase of the DOS for ABC-stacked PTTA appears further away from band edge at around 0.15 eV.

Electrical conductivity and electronic thermal conductivity

The electrical conductivity σ and electronic thermal conductivity κ_e, which strongly depend on the carrier concentration, are shown in Figure S9 for p-type and n-type doping.

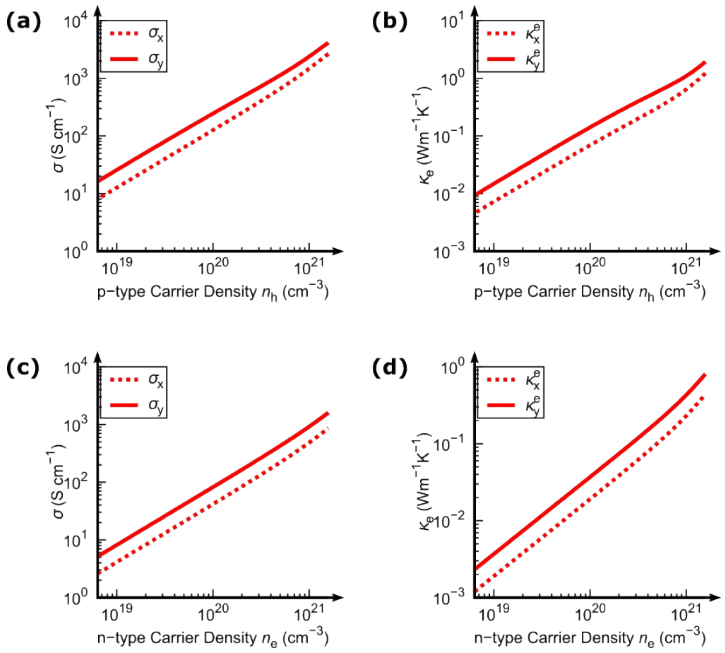

Figure S9. Carrier concentration dependence of **(a)** electrical conductivity and **(b)** electronic thermal conductivity for p-type carriers. **(c)** and **(d)** are electrical and electronic thermal conductivity for n-type carriers.

Due to the relatively small carrier mobility, the electrical conductivity at high doping level is not very large, around the order of 10^2 S cm^{-1}. The electronic contribution to thermal conductivity is lower than 1 W m^{-1} K^{-1}, which is within the commonly observed range for polymer materials[3].

Temperature dependence of transport properties

The doping level dependent transport coefficients, including Seebeck coefficients S, Hall mobility μ_H, electrical conductivity σ, electronic thermal conductivity κ_e, and power factor PF, are calculated at different temperatures of 200 K, 250 K, 300 K, 350 K, and 400 K. The results for p-type doping are given in Figure S10 and n-type doping in Figure S11.

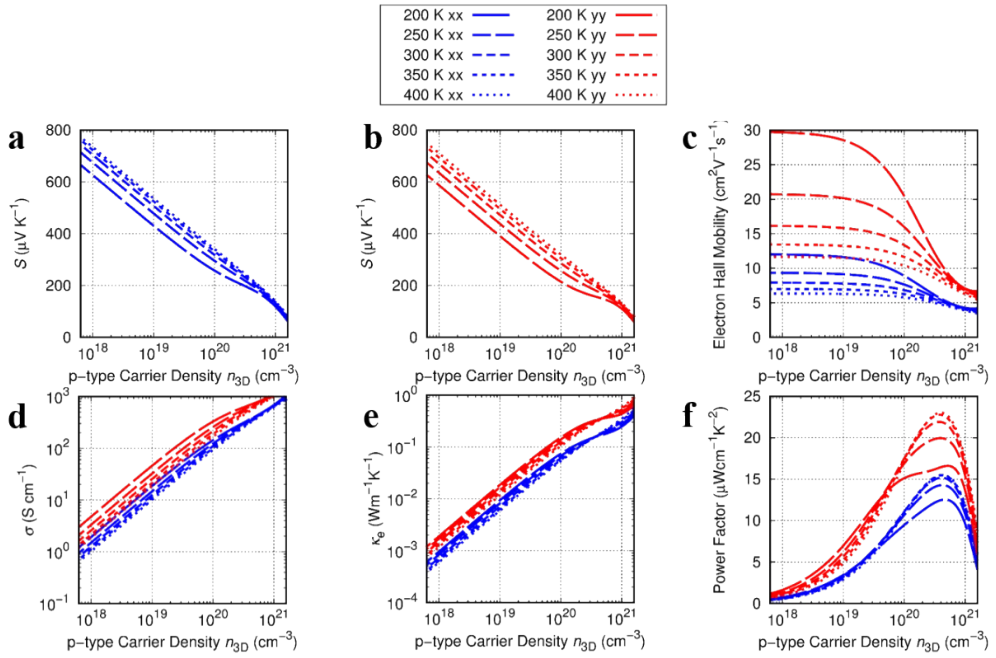

Figure S10 Temperature and doping level dependent transport coefficients for p-type doping.

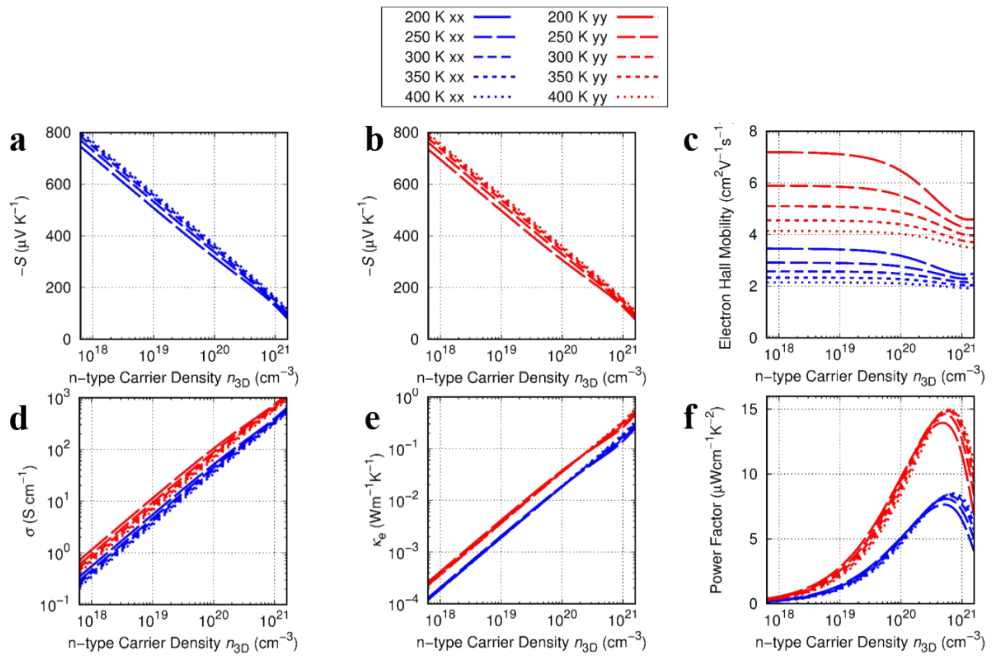

Figure S11 Temperature and doping level dependent transport coefficients for n-type doping.

The general trend, for both p-type and n-type doping, is that the Seebeck coefficient is enhanced as temperature increases. This can be understood through activation of high energy carrier at higher temperature, similar to the energy-filtering effect[4]. Meanwhile, the carrier mobility at low doping level are significantly suppressed as a result of higher population of phonons, where electron-phonon scattering dominates. At higher doping level, impurity scattering is stronger and competes with electron-phonon scattering. The temperature dependence at high doping level is therefore less noticeable because electron-impurity scattering is elastic and not sensitive to temperature. This leads to decreased conductivities as temperature increases. The combination of these effects towards the Seebeck coefficient and carrier mobility leads to decreased power factor at low doping level and increased power factor at high doping level.

Methods

First principles calculations: Electron band dispersion, phonon dispersions and electron-phonon couplings are calculated using the density functional perturbation theory (DFPT)[5,6] with Perdew, Burke and Ernzerhof's (PBE) generalized gradient approximation (GGA)[7] as implemented in PHONON package of Quantum ESPRESSO[8,9]. A set of optimized norm-conserving Vanderbilt

pseudopotentials from PseudoDojo[10] are used to replace core electrons. A plane-wave cut-off energy of 90 Ry together with a uniform 3×3×1 Brillouin zone sampling mesh is used. A vacuum layer of 10 Å is used for both PTTA and its isomer to avoid interaction between periodic images. Then the electron energy dispersion, phonon dispersion and electron-phonon matrix elements are interpolated into a finer 60×60×1 mesh using maximally localized Wannier functions[11,12] as implemented in Electron-Phonon coupling using Wannier functions (EPW)[13] to evaluate the carrier lifetime.

To evaluate the relaxation time from first principles, we calculated the electron lifetime due to electron-phonon interaction and used it to approximate electron relaxation time[12] as

$$\tau_{nk}^{-1} = \frac{2\pi}{\hbar N_q}\sum_{m\lambda q}\left|g_{nm\lambda}(k,q)\right|^2\left[\left(1-f_{mk+q}^{0}+n_{\lambda q}^{0}\right)\delta\left(\varepsilon_{nk}-\hbar\omega_{\lambda q}-\varepsilon_{nk+q}\right)+\left(f_{mk+q}^{0}+n_{\lambda q}^{0}\right.\right. \quad (1)$$

where $\hbar$, N_q, $g_{nm\lambda}(k,q)$, f_{mk+q}^{0}, ε_{nk}, $n_{\lambda q}^{0}$, and $\omega_{\lambda q}$ stand for reduced Planck constant, number of q points, electron-phonon matrix element, Fermi-Dirac distribution, electron energy, Bose-Einstein distribution, and phonon frequency, respectively.

To estimate the impact of charged impurity scattering, we consider screened Coulombic impurity with effective charge $Z^* = Z/\varepsilon_r$. The scattering matrix elements are given by[14,15]

$$M_{nk,mk+q} \approx \frac{e^2}{4\pi\epsilon_0}\left|\frac{2\pi\langle u_{mk+q}\,|\,u_{nk}\rangle}{\Omega\,|q+G|+q_{TF}}\right|_{G+q\in 1BZ} \quad (2)$$

with e, ϵ_0, Ω, and k, k' and q_{TF} being elementary charge, vacuum permittivity, sample area, crystal momenta of initial and final states, and Thomas Fermi screening wave vector, respectively. The screening wave vector $q_{TF} = \frac{e^2}{2\epsilon_0}D_0$ is determined by the band edge density of states D_0. Their contribution to scattering rate is given by

$$\tau_{nk}^{-1} = \frac{2\pi}{\hbar}n_i^*\sum_{mq}\frac{1}{N_q}\left|M_{nk,mk+q}\right|^2\left(1-\cos\theta_{nk,mk+q}\right)\delta\left(\varepsilon_{nk}-\varepsilon_{mk+q}\right) \quad (3)$$

where the effective impurity density is $n_i^* = n_i(Z^*)^2$, Ω_{BZ} is the area of the first Brillouin zone, and ε_k is the energy of electron with crystal momentum k. The $\cos\theta_{kk'}$ term is taken to be $\frac{v_k \cdot v_{k'}}{v_k \cdot v_k}$ [16] while other definitions are also seen in literature[15]. Assuming charge neutrality in the whole system, we consider monovalent impurity with density equal to the corresponding carrier concentration.

Molecular dynamics: Ab initio molecular dynamics simulation was carried out using Vienna Ab initio Simulation Package (VASP)[17]. A kinetic energy cutoff of 400 eV for the plane-wave basis set and projector augmented-wave (PAW)[18] pseudopotentials were used for all molecular dynamics simulations. Simulations were performed in NVT ensemble at 300 K and 600 K respectively. The simulation durations were 13 ps for 300 K and 6 ps for 600 K where convergence is achieved, and the time step size was 1 fs.

Boltzmann transport equations: To theoretically evaluate the TE performance, BTE was employed to calculate electrical conductivities and Seebeck coefficients. The electron velocity matrix is evaluated in local approximation and the diagonal part v_{nk} is used to calculate the electrical conductivity tensor σ and Seebeck coefficient tensor S in single mode relaxation time approximation using[19]

$$\sigma_{\alpha\beta} = \frac{G_s e^2}{N_k \Omega} \sum_{nk} v_{nk}^{\alpha} v_{nk}^{\beta} \tau_{nk} \left[-\frac{\partial f^0(\varepsilon)}{\partial \varepsilon} \bigg|_{\varepsilon = \varepsilon_{nk} - \mu} \right] \tag{4}$$

$$(\sigma S)_{\alpha\beta} = \frac{G_s(-e)}{N_k \Omega T} \sum_{nk} v_{nk}^{\alpha} v_{nk}^{\beta} \tau_{nk} \left[-\varepsilon \frac{\partial f^0(\varepsilon)}{\partial \varepsilon} \bigg|_{\varepsilon = \varepsilon_{nk} - \mu} \right] \tag{5}$$

Here, $\sigma_{\alpha\beta}$ and v_{nk}^{β} are the components of tensor σ and vector v_{nk}, respectively, G_s is spin degeneracy, and N_k is the number of k-points. The carrier mobility $\mu_{\alpha\beta}$ is obtained from the ratio between $\sigma_{\alpha\beta}$ and carrier concentration.

Two-dimensional effective mass model: Assuming a parabolic dispersion in two-dimensional system where $\varepsilon_k = \frac{\hbar^2 k^2}{2m^*}$, the density-of-states for single band is

$$D(E) = G_s \sum_{nk} \frac{1}{N_k} \delta\left(E - \frac{\hbar^2 k^2}{2m^*}\right) = \frac{G_s A |m^*|}{2\pi \hbar^2} \tag{6}$$

with A being the unit cell area.

In this approximation, the transport coefficient in constant relaxation time approximation becomes

$$L_{\alpha\beta}(E) = \frac{G_s}{N_k \Omega} \tau \sum_k v_k^\alpha v_k^\beta \delta(E - \varepsilon_k) = \frac{G_s \tau}{2\pi\hbar^2} \delta_{\alpha\beta} H(E) E \tag{7}$$

Here, $H(E)$ is the Heaviside step function. Then, we have the conductivity

$$\sigma_{\alpha\beta} = e^2 \int_0^\infty L_{\alpha\beta}(E) \left[-\frac{\partial f^0(E-\mu)}{\partial E} \right] dE = \delta_{\alpha\beta} \frac{\tau e^2}{|m^*|} n_e \tag{8}$$

The corresponding Hall mobility is simply $\mu_H = \frac{\tau |e|}{|m^*|}$, and the Seebeck coefficient comes in a simple relation with Fermi level and temperature as

$$S_{\alpha\beta} = \frac{1}{Te} \frac{2k_B T \, Li_2\left(-e^{\mu/k_B T}\right) - \mu Li_1\left(-e^{\mu/k_B T}\right)}{Li_1\left(-e^{\mu/k_B T}\right)} \tag{9}$$

where $Li_n(x)$ is the polylogarithm function of order *n*.

Structural Information

The lattice parameters and atomic positions are given here.

PTTA:

Primitive cell vectors in Angstrom:

7.0353830866	-9.7884874837	0.0000000000
7.0353830866	9.7884874837	0.0000000000
0.0000000000	0.0000000000	10.0000000000

Atomic positions in Angstrom:

C	-0.7178783484	-6.0656306681	0.0000000000
C	0.7178783484	6.0656306681	0.0000000000
C	0.7178783484	-6.0656439280	0.0000000000
C	-0.7178783484	6.0656439280	0.0000000000
C	1.3927124686	-7.2967681616	0.0000000000
C	-1.3927124686	7.2967681616	0.0000000000
C	-1.3927136740	-7.2967741888	0.0000000000
C	1.3927136740	7.2967741888	0.0000000000
C	0.7233836410	-8.5619994130	0.0000000000
C	-0.7233836410	8.5619994130	0.0000000000
C	-0.7233836410	-8.5619945912	0.0000000000
C	0.7233836410	8.5619945912	0.0000000000
C	-1.6022306229	4.9565643297	0.0000000000
C	1.6022306229	-4.9565643297	0.0000000000
C	1.6022450883	4.9565848224	0.0000000000
C	-1.6022450883	-4.9565848224	0.0000000000
C	-2.9360568322	5.3186165800	0.0000000000
C	2.9360568322	-5.3186165800	0.0000000000
C	2.9360339286	5.3186153745	0.0000000000
C	-2.9360339286	-5.3186153745	0.0000000000
C	5.6379380192	-0.0000024109	0.0000000000
C	-5.6379380192	0.0000024109	0.0000000000
S	-3.9240862919	2.7300429227	0.0000000000
S	3.9240862919	-2.7300429227	0.0000000000
S	3.9240862919	2.7300429227	0.0000000000
S	-3.9240862919	-2.7300429227	0.0000000000
H	-1.2752690381	3.9193307895	0.0000000000
H	1.2752690381	-3.9193307895	0.0000000000
H	1.2752666272	3.9193211459	0.0000000000
H	-1.2752666272	-3.9193211459	0.0000000000
H	4.5469413845	-0.0000000000	0.0000000000
H	-4.5469413845	0.0000000000	0.0000000000

Isomer:

Primitive cell vectors in Angstrom:

7.6755470172	8.6750413987	0.0000000000
-7.6755470172	8.6750413987	0.0000000000
0.0000000000	0.0000000000	10.0000000000

Atomic positions in Angstrom:

C	0.7195057774	9.9001369932	0.0000000000
C	-0.7195057774	7.4499565499	0.0000000000
C	-0.7195057774	9.9001369932	0.0000000000
C	0.7195057774	7.4499565499	0.0000000000

C	1.4241209936	6.1892986110	0.0000000000
C	-1.4241209936	11.1607949322	0.0000000000
C	-1.4241209936	6.1892986110	0.0000000000
C	1.4241209936	11.1607949322	0.0000000000
C	0.7050757490	4.9772207442	0.0000000000
C	-0.7050757490	12.3728712638	0.0000000000
C	-0.7050757490	4.9772207442	0.0000000000
C	0.7050757490	12.3728712638	0.0000000000
C	-3.1807466839	12.7217816748	0.0000000000
C	3.1807466839	4.6283103332	0.0000000000
C	3.1807466839	12.7217816748	0.0000000000
C	-3.1807466839	4.6283103332	0.0000000000
C	-2.8252153461	11.3858250845	0.0000000000
C	2.8252153461	5.9642684586	0.0000000000
C	2.8252153461	11.3858250845	0.0000000000
C	-2.8252153461	5.9642684586	0.0000000000
S	-1.7592353763	13.7468264172	0.0000000000
S	1.7592353763	3.6032671259	0.0000000000
S	1.7592353763	13.7468264172	0.0000000000
S	-1.7592353763	3.6032671259	0.0000000000
H	-3.5683618083	10.5920583897	0.0000000000
H	3.5683618083	6.7580351534	0.0000000000
H	3.5683618083	10.5920583897	0.0000000000
H	-3.5683618083	6.7580351534	0.0000000000
C	1.3944933821	8.6750460040	0.0000000000
C	-1.3944933821	8.6750460040	0.0000000000
H	2.4825789272	8.6750460040	0.0000000000
H	-2.4825789272	8.6750460040	0.0000000000

Reference

(1) Grimme, S. Semiempirical GGA-Type Density Functional Constructed with a Long-Range Dispersion Correction. *J. Comput. Chem.* **2006**, *27* (15), 1787–1799.

(2) Grimme, S.; Antony, J.; Ehrlich, S.; Krieg, H. A Consistent and Accurate Ab Initio Parametrization of Density Functional Dispersion Correction (DFT-D) for the 94 Elements H-Pu. *J. Chem. Phys.* **2010**, *132* (15), 154104.

(3) Wang, H.; Yu, C. Organic Thermoelectrics: Materials Preparation, Performance Optimization, and Device Integration. *Joule* **2019**, *3* (1), 53–80.

(4) Dresselhaus, M. S.; Chen, G.; Tang, M. Y.; Yang, R. G.; Lee, H.; Wang, D. Z.; Ren, Z. F.; Fleurial, J.-P.; Gogna, P. New Directions for Low-Dimensional Thermoelectric Materials. *Adv. Mater.* **2007**, *19* (8), 1043–1053.

(5) Gonze, X. Adiabatic Density-Functional Perturbation Theory. *Phys. Rev. A* **1995**, *52* (2), 1096–1114.

(6) Baroni, S.; De Gironcoli, S.; Dal Corso, A.; Giannozzi, P. Phonons and Related Crystal Properties from Density-Functional Perturbation Theory. *Rev. Mod. Phys.* **2001**, *73* (2), 515–562.

(7) Perdew, J. P.; Burke, K.; Ernzerhof, M. Generalized Gradient Approximation Made Simple. *Phys. Rev. Lett.* **1996**, *77* (18), 3865–3868.

(8) Giannozzi, P.; Baroni, S.; Bonini, N.; Calandra, M.; Car, R.; Cavazzoni, C.; Ceresoli, D.; Chiarotti, G. L.; Cococcioni, M.; Dabo, I.; et al. QUANTUM ESPRESSO: A Modular and Open-Source Software Project for Quantum Simulations of Materials. *J. Phys. Condens. Matter* **2009**, *21* (39), 395502.

(9) Giannozzi, P.; Andreussi, O.; Brumme, T.; Bunau, O.; Buongiorno Nardelli, M.; Calandra,

M.; Car, R.; Cavazzoni, C.; Ceresoli, D.; Cococcioni, M.; et al. Advanced Capabilities for Materials Modelling with Quantum ESPRESSO. *J. Phys. Condens. Matter* **2017**, *29* (46), 465901.

(10) van Setten, M. J.; Giantomassi, M.; Bousquet, E.; Verstraete, M. J.; Hamann, D. R.; Gonze, X.; Rignanese, G.-M. The PseudoDojo: Training and Grading a 85 Element Optimized Norm-Conserving Pseudopotential Table. *Comput. Phys. Commun.* **2018**, *226*, 39–54.

(11) Giustino, F.; Cohen, M. L.; Louie, S. G. Electron-Phonon Interaction Using Wannier Functions. *Phys. Rev. B* **2007**, *76* (16), 165108.

(12) Giustino, F. Electron-Phonon Interactions from First Principles. *Rev. Mod. Phys.* **2017**, *89* (1), 15003.

(13) Poncé, S.; Margine, E. R.; Verdi, C.; Giustino, F. EPW: Electron–phonon Coupling, Transport and Superconducting Properties Using Maximally Localized Wannier Functions. *Comput. Phys. Commun.* **2016**, *209*, 116–133.

(14) Ando, T.; Fowler, A. B.; Stern, F. Electronic Properties of Two-Dimensional Systems. *Rev. Mod. Phys.* **1982**, *54* (2), 437–672.

(15) Das Sarma, S.; Adam, S.; Hwang, E. H.; Rossi, E. Electronic Transport in Two-Dimensional Graphene. *Rev. Mod. Phys.* **2011**, *83* (2), 407–470.

(16) Grimvall, G. *The Electron-Phonon Interaction in Metals*; Series of monographs on selected topics in solid state physics; North-Holland Publishing Company : sole distributors for the U.S.A. and Canada, Elsevier North-Holland, 1981.

(17) Kresse, G.; Furthmüller, J. Efficient Iterative Schemes for Ab Initio Total-Energy Calculations Using a Plane-Wave Basis Set. *Phys. Rev. B* **1996**, *54* (16), 11169–11186.

(18) Blöchl, P. E. Projector Augmented-Wave Method. *Phys. Rev. B* **1994**, *50* (24), 17953–17979.

(19) Mahan, G. D.; Sofo, J. O. The Best Thermoelectric. *Proc. Natl. Acad. Sci.* **1996**, *93* (15), 7436–7439.